Grant agreement no. 312818

SPA.2012.2.2-01 : Key technologies enabling observations in and from space

- Collaborative project -

WP 3 – Interferometer Instrument Technology Development

D3.7
Final Report on Instrument technology readiness for a FIR interferometer

Due date of deliverable: month 36

Actual submission date:

Start date of project: January 1ˢᵗ 2013   Duration: 36 months

Lead beneficiary for this deliverable: UCL

Last editor: G.Savini, University College London (UCL)

Contributors:
G. Savini (UCL).

Project co-funded by the European Commission within the Seventh Framework		
Dissemination Level (please refer to the list of deliverables in Annex 1 and complete		
PU	Public	■
PP	Restricted to other programme participants (including the Commission	
RE	Restricted to a group specified by the consortium (including the	
CO	Confidential, only for members of the consortium (including the Commission Services)	

History table

Version	Date	Released by	Comments
0.1		UCL	First issue
0.2		NUIM	Added optical modelling contributions
0.3		Cardiff University	First draft of testbed and how elements affect the data
1.0		UCL	Data description and basics of data pipeline
1.3	12/1/2016	Cardiff	Final formatting, Bibliography
1.4	14/1/2016	Cardiff	Final cleanup.

Table of contents

Acknowledgements

Disclaimer

The content of this deliverable does not reflect the official opinion of the European Union. Responsibility for the information and views expressed in the deliverable therein lies entirely with the author(s).

1 Introduction

1.1 General context

In the formulation of the original Description of Work for Workpackage 3, it was envisioned that after the upgrade of the testbed (described in D3.4) and the data analysis of subsequent runs to assess the performance of the testbed, non-linearity of the detector response and of the phase delay would impact the information recovery. As such the deliverable description was worded. Subsequently, with more in-depth analysis of the data, it became apparent that detector non-linearity was not a significant issue, but that other instrumental effects or component non-ideal behaviour impacted the data. We therefore aim to give an account of our findings in the data analysis of the data runs and the effects which are potentially the cause of limitation for this technique in this document.

1.2 Deliverable description

From the Description of Work this deliverable has the purpose of reporting on spectral spatial reconstruction with results of linearity tests. Describing the optical performance, positioning tolerances and phase errors associated with the test data runs using the Cardiff test bed. Here we include the data algorithms used to process the data and the implications of our findings with a description of the subsequent steps which will be investigated following the end of this activity.

1.3 Deliverable objectives

The objective of this deliverable is to provide a basic but detailed understanding of how the data is produced in the spectral-spatial interferometry testbed in Cardiff, what are the techniques used to process the data and how this is then reduced to obtain the original source picture. It is critical that the objective of clearly explaining how the data analysis is performed and what the hardware issues are is reached in order to serve as a reference for any groups engaging with this technique on problems to avoid and possibly methods to employ.

1.4 Document structure

In the first part we summarize the way in which the testbed data is produced and its nature. This will necessarily produce a multiple set of references to deliverable D3.4. In the following section we describe the data pipeline used as well as the formalism which would be adopted in a blind approach. In the final two sections we discuss the detailed optical model of the testbed and the implications to future builds and data analysis as well as a number of non-idealities which have potential impact and that need further study or improvements.

2   Spectral-spatial interferometry testbed data.

The testbed described in D3.3 and upgraded as described in section 1.4 of the same document produces data recorded by a single pixel detector. In this section we discuss the nature of the data and the various elements of the testbed that affect them. To do this we follow the path of the photons ultimately recorded by the detector in their journey from the source used.

2.1   The source

A water-cooled mercury arc lamp is used as the radiation source. It produces a nearly uniform emission over a 10mm diameter area which allows the use of a multiple aperture screen to be placed in front of it to simulate a range of sources in a predefined configuration. This sky scene aperture is located at the focus of a large collimating mirror such that the source scene mimics an astronomical scene of stellar like objects located at infinity. The source has a colour temperature T ~ 2000 K and has a continuum spectrum which is close to that of a blackbody.

2.2   The collimator

The large collimator is one of six segments of a carbon fibre mirror originally used for the 2m diameter balloon-borne BLAST telescope. The telescope was damaged during recovery operations post-flight but the segments were recovered and have since been re-deployed for laboratory use. The segment has a spherical curvature with a 4m radius of curvature and hence has an effective focal length ~2m. It has an equilateral triangular shape with a 1m base – so is ideal for illuminating the two telescopes of our scanning interferometer which have baseline coverage of 400mm. The plate scale at the prime focus (the location of the sky scene aperture) is 1.64 arcmin/mm. As will be discussed later on the panel is flexible and although it is supported at three points small microphonic driven flexing (~5μm) caused noticeable phase noise. This is one area where with the addition of a stiff backplate the interferometer could gain in both phase stability and S/N.

2.3   The telescopes (antennas)

The light from the collimator is in the far field of two telescope units or antennas. One is fixed to the bench. The other can be linearly translated with respect to the first antenna to affect the interferometer baseline. The actual mechanical motion is 300mm which when taken with the 101.6mm diameter of each telescope unit translates to a minimum baseline of 100mm and a maximum of 401.6mm.
Each telescope unit consists of a pair of off-axis parabolic mirrors to provide a condensed, collimated beam at the input of the interferometer. In this way a plane parallel incident beam is translated to a nearly plane parallel output beam but with its diameter reduced by the ratio of focal lengths of the two parabolic mirrors. For the mirrors used in the test-bed, this ratio is 2.4. Thus the input telescope beam is reduced to 42.3mm at the telescope unit output (see D3.3 for details).   Because the output beam is not perfectly collimated we adjusted the telescope mirror unit separation to provide a 42.3mm image at the beam combiner to ensure good overlap of the two ports of the interferometer.

2.4   The delay stage

The optical delay line is actuated using an Aerotech ALS1000 Mechanical-Bearing Direct-Drive linear stage which provides an equal-space sampling trigger signal (sampling precision ≤ 100nm) which is used to trigger the data acquisition systems. The total travel of the stage is 450 mm, allowing it to be used to compensate the delay introduced by the varying baseline separation between the two antennae (up to 300 mm) and to obtain interferograms to retrieve the spectral information by rapid scanning about each compensated zero path difference, zpd, position. The high absolute positional accuracy (resolution 50nm with repeatability of 1.0μm) of

the ALS1000 enabled interferogram averaging at each baseline to reduce 1/f noise arising from a combination of photon noise, phase noise and variations in the atmospheric opacity. The second port path compensation requires that the FTS scanning mirror is repositioned by half the baseline change. So for the maximum baseline travel we need to compensate the scanning mirror by 150mm. This leaves (450-150)/2=150mm (to ensure we can scan the spectrum at the extreme baselines) as the maximum scanning distance of the FTS. So the maximum achievable spectral resolution for our testbed is $\Delta v = 1/(2 \times$ scan distance) or 0.0033 cm^{-1}. This is far greater than is needed for our laboratory tests so we limited the FTS scan to 2cm opd or 0.5 cm^{-1} which is more than sufficient to resolve the atmospheric absorption lines and for a given observation time provides high S/N spectra.

The bolometric detector used has a time constant ~ 1msec allowing a rapid scan velocity of 0.5cm/sec in optical path difference for the highest frequency band observed (25µm). With this velocity the spectral frequencies over the band (350 – 450 cm^{-1}) translate to detector frequencies between 175 and 225 Hz well within the frequency range of the bolometer. For the long waveband the drive speed can be increased to move the spectral signatures away from the 1/f low frequency detector noise.

2.5   The beam combiner

Two different beam combiners have been designed and manufactured using Cardiff metal mesh fabrication facility. One operates in the 5-33cm-1 region while the second unit is optimised for measurements at higher frequencies covering the 80 – 580cm^{-1} region which encompasses the 25µm atmospheric window. The measured properties (transmission and reflection) are shown in Figure 1 and are discussed further in D3.2 and D3.3.
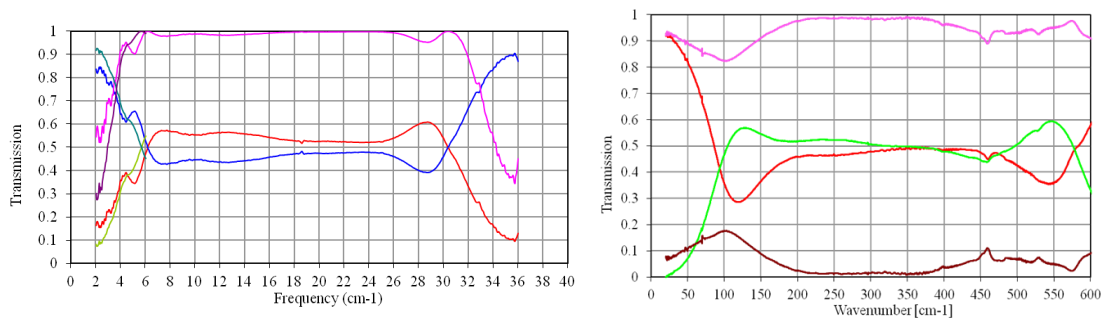
Figure 1: left - Measured transmission and reflection for the beam divider covering the 5 – 33cm-1 region. Red curve is transmission; blue is reflection and pink is 4RT. Right - Measure data for the higher frequency beam divider developed for working in the 25µm region. Red curve is reflection, green is transmission, brown is absorption and pink is 4RT

2.6   The coupling optics.

The output collimated beam from the interferometer is focussed by a parabolic mirror onto a horn coupled bolometric detector. This is a F/4.5 parabolic horn with a 2 mm exit aperture and a 3mm entrance aperture.

To limit unwanted background IR radiation filters are placed at the horn entrance and on the cryostat radiation shield (see white disc on shield in Figure 2).
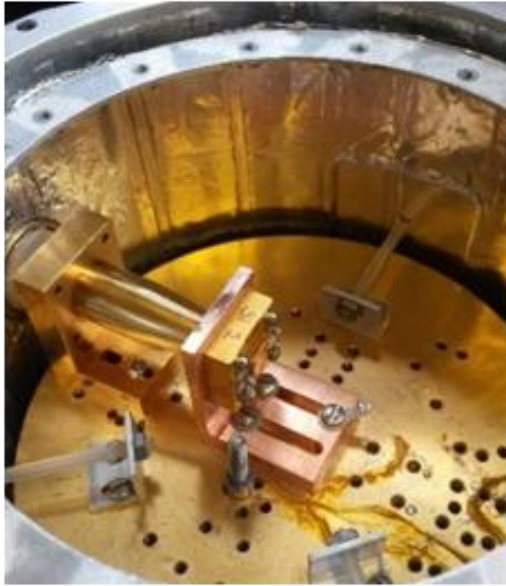
Figure 2: The silicon bolometer detector assembly on the cryostat cold plate. The feed horn and detector block are visible viewing though a window on the outer vacuum can.

For 1THz region a lowpass 33cm^{-1} filter was used at the horn entrance and for the 25µm region a bandpass filter was used. Both filters were manufactured at Cardiff. The measure profile of the bandpass filter is shown in Figure 3.
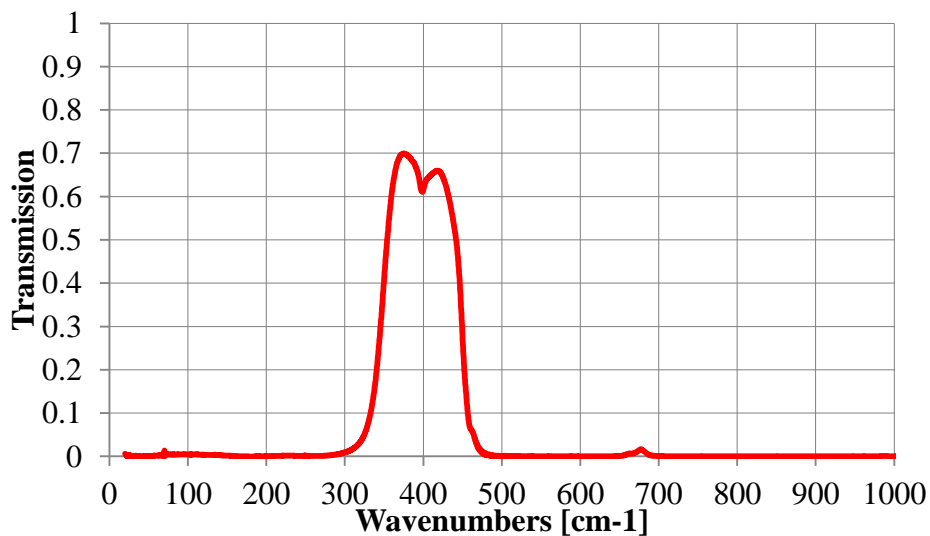
Figure 3. Transmission of 25µm bandpass filter.

2.7   The detector

A silicon bolometric detector was chosen for the initial measurements because it can be operated at 4K in a small cryostat which is easily accommodated on the interferometer bench. As discussed above, band selection filters are used in the cryostat at 4K in order to define the spectral region of operation and limit the FIR flux to maximise the signal to noise. The detector time constant also enabled rapid scanning as described above which modulated the wanted signals at a few hundred hertz mitigating low frequency atmospheric fluctuation and inherent detector noise issues. This detector has a modest thermal conductance which ensures that for the signal dynamic range encountered here

that its response is linear whilst providing an optical NEP referred to the cryostat 300K window of ~1.10^{-12} W.Hz$^{-1/2}$.

This is close to but not at the photon noise limit so an improvement could be made by using photodetectors optimised to the wanted photometric band in the future.

3   Spectral-spatial Interferometry data pipeline and blind processing.

This chapter outlines how the data is acquired and how it is processed in order to provide a clear view of the analysis performed and other possible ways of data processing.

3.1   The data sets acquired

Explain the parameter space explored for the data set being discussed in the data pipeline description.

The data sets acquired are from a single detector receiver (4K silicon bolometer) which has a fast (~1 ms) time constant via a National Instruments card and is visualized in real time via Labview software on a desktop PC.

The same Labview software interface allows the user to set the testbed parameters dictating what data sets to acquire. These are specifically:

> (A) Spectral: OPD scan sample [Δx]
> (B) Spectral: Max OPD [L]
> (C) Spectral: Scanning speed [v_{FTS}]
> (D) Spatial: Initial baseline separation [b_0]
> (E) Spatial: Baseline length step [db]
> (F) Spatial: Number of baselines [n_b]

The first three parameters dictate the spectral information content that will be acquired by the detector, the latter three the equivalent for the spatial information.

(A) and (B) dictate the number of points sampled in an interferogram (IG) and combining (A) and (C) yields the sampling frequency of the detector.

For example data sets acquired for the data shown in [1] has $n_p = 26000$ points acquired with $\Delta x = 1.6 \ \mu m$ for a total $L = 4.16 \ cm$. The corresponding Nyquist frequency (where aliasing in the spectral domain ensues is $v_{Nyq} = \frac{1}{(2\Delta x)} = 3125 \ cm^{-1}$ which is plenty of margin given that the expend band (given the measured band-pass filter center to be at $\sim 400 \ cm^{-1}$.

The resulting spectrum obtained by taking the absolute value of the Fast Fourier Transform applied to the discrete set of points is shown in Figure 4. The vector of wavenumbers used for the x-axis representation is defined as a vector of n_p points with a wavenumber resolution of is $\Delta v = \frac{2v_{Nyq}}{n_p} \cong 0.24 \ cm^{-1}$.

As we can see, the spectrum is where we expect it to be having previously measured the band-pass filter employed in the detector system. With the exact band-defining edges (at 10% of peak power) being [360,460] cm^{-1}, which inversely and swapped correspond to [21.7,27.8] μm.

An interesting verification process can be performed looking at the noise features observed in the spectra. 3 lines appear in the spectra respectively at 25, 50 and 150 cm^{-1}.

Let us consider the 50Hz mains noise source. How will this contaminate the spectrum in our case? The link between temporal or frequency related noise is translated in wavenumber space given the optical sampling speed which ties sampling frequency to a physical length. In such way, our speed $v = 1.0 \ cm \cdot s^{-1}$ transduces $f = 50 \ Hz$ into $v_{mains} = f/v = 50 \ cm^{-1}$ which is exactly where our noise peak presents itself.

The remaining two features can either be considered as similar electrical disturbances occurring respectively at 25 and 150Hz, or other quantities which can mechanically affect the testbed such as the periodic beat generated by a non perfectly circular or uniform lead screw

rotation (not the case for this Aerotech stage). Another source of noise which could have affected the data are mechanical vibrations such as the water-cooler which runs in the proximity to maintain the Hg-arc lamp source at a stable temperature.
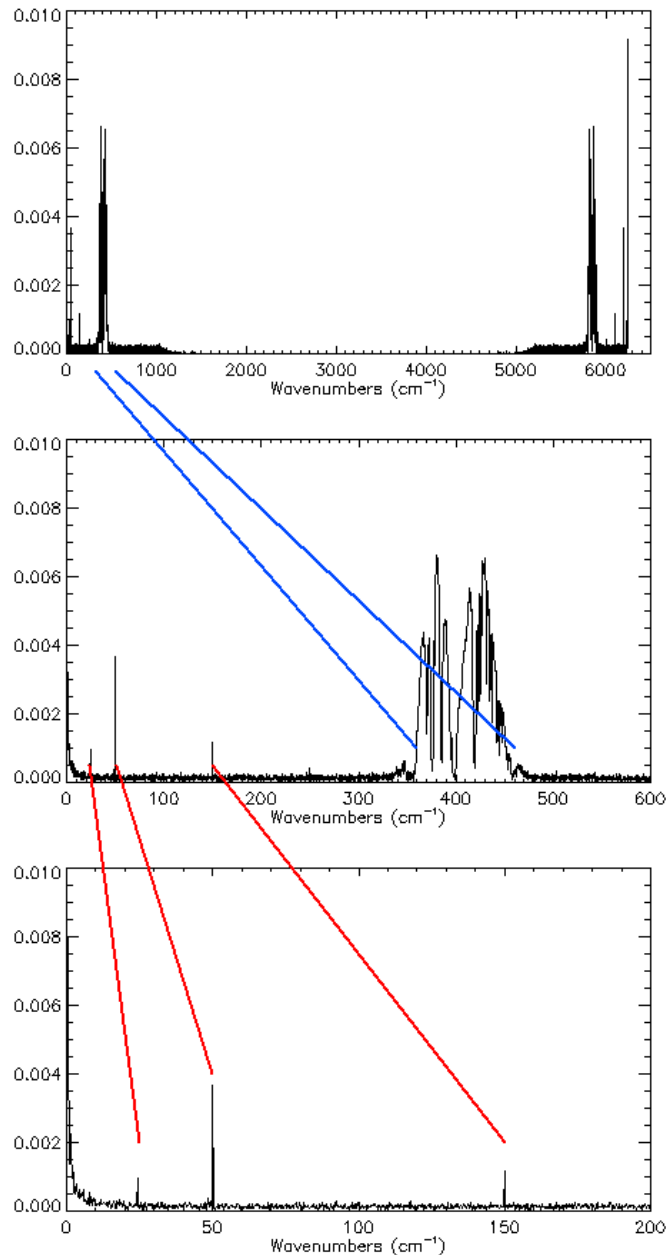
Figure 4. All 3 plots are the same with the top one showing the entire Fast Fourier Transform applied to the discrete set of points acquired as explained in the example in 3.1. (Middle) Zoom of the interesting part of the spectrum (where power is allowed in the system), showing how the spectrum matches the expected power input at the frequencies corresponding to the band –pass filter employed. (bottom) Noise features as explained in the text.

In addition to the sources of noise, we perform a check in band with features which are caused by the presence of water vapor in the lab (which is a nuisance generally) but has the one advantage to be able to pinpoint accurately the positioning of the water lines and thus verify spectral calibration.

The number of water vapor lines in this region allows us to do a conservative check on the data in hand which is shown in Figure 5. We have generated a MODTRAN (v5.3) standard T and P profile including water lines for a laboratory environment and optical path of 4 meters. This

was then scaled in order to appear fitting inside the band-passing spectrum detected by our system.
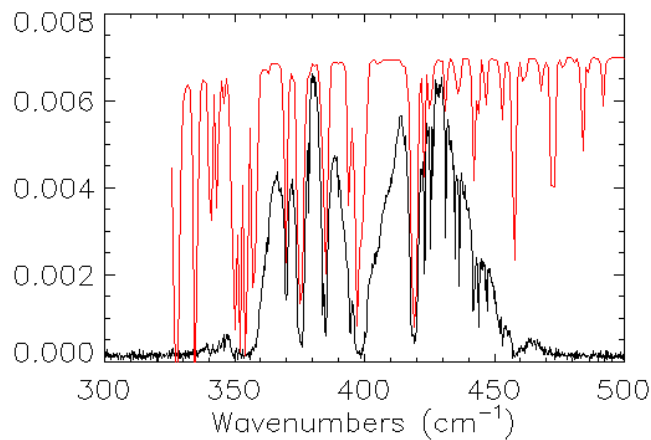
Figure 5. Overlap of Spectrum for the source, superimposed to a MODTRAN generated spectral profile. The position of the sharp water lines can be observed matching in spectrum and model.

Of the data sets analyzed we effectively focused on the best sets obtained where careful alignment of the source and all other optical components was achieved after the upgrade of the testbed components. As such, we use as reference a single slit source run which we refer as SS (from the May15 run), a double-slit run which we refer to as DS (Feb15) where only a smaller range of baselines is available due to progressively decreasing sensitivity as the Liquid helium reserves were running low. There are other data sets (single and double slots) which were either inferior in quality of with other system parameters holding values which while still allowing the basic analysis for source recovery, did not offer additional insights in the analysis.

It is indeed from the best data sets which we have gleaned effects that point to first order non-ideal performance in the elements that constitute the testbed.

3.2   The data analysis performed

Once the data is acquired, this is presented as interferograms. A forward and backward for each baseline. Note that this is actually the result of a number of averages performed to reduce the statistical noise of the single scans.

The amounts of scan is another parameter input in the labview control software but has no other implication at this level than that of reducing noise. In Figure 6 we show an entire interferogram where the larger signal is where the bright region of the source is closer to its ZPD (zero-path-difference).

Data analysis can be performed with different goals. While the prime goal has been initially that of validating the testbed performance and the demonstration of spatial-spectral interference, there is also the need to migrate to a "blind" reconstruction of the calibration scene which is ultimately what the instrument would be doing if observing with a large number of baselines without prior knowledge of the source it is observing (this compatibly with the prior knowledge of the source which is used when performing interferometry).

We will describe briefly here the three separate techniques which we have employed in different instances for data analysis from the early stages of the Grainger et al. paper (time

domain forward modelling), the manual spatial reconstruction via spectral binning and forward modelling of the source, and the associated Monte-Carlo best-fit of the source scene (adopted for the latest conference proceedings where the data was presented) and finally we describe the data algorithms employed in the "blind" reconstruction of the simulated scenes for FIInS.
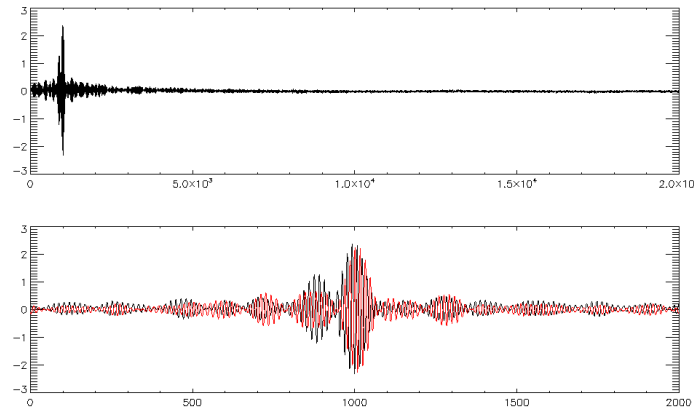
Figure 6. (Above) An interferogram taken from the DS set. The area closer to the Zero-Path difference of the bright region of the source is visible to the left of the scan. (Below) Zoomed in the ZPD region, in red, the overlapped scan taken 10 baselines further apart. The shift in ZPD is apparent from the mis-match of the central region but more importantly the lower fringe amplitude on the second highest amplitude shows the difference in fringe visibility pattern due to the spatial modulation.

This latter approach has one non-trivial difference with the experimental data which is the sampling (regardless of the two-dimensional nature) of both sides of the axis.

This technique has not been successful yet (in our case) to reproduce decent quality 1-D cuts of the source in post-processing. Discussion on future efforts to tackle "blind" approaches and image reconstruction will be mentioned in the conclusions of this document.

3.2.1 Time domain forward modelling

This method was employed for the initial validation of the spectral-spatial interferometry experiment performed in Grainger et al. where we had previously measured the spectra of the source adopted and had furthermore the prior knowledge that the two sources involved possessed the same spectra.

More precisely, it is not the exact prior knowledge of the spectral content of the source which is required but an FTS equivalent (i.e. single antenna with a 50/50 beam splitter as well as the beam combiner) set of data in the form of the IG. As this is the Fourier transform of the true spectrum of the source, this is what is obtained if this point source was at infinity and perfectly symmetrical on the axis of the two telescope baseline.

With this assumption in place any interferogram acquired from a source which is the same but presents a mask separating its spatial contributions can be modelled by co-adding the same IG in a linear combination after applying a time-domain shift to the IG caused by the equivalent angular separation of the different parts of the source.

In the case of the two slit spectra of the Grainger et al. the resulting interferogram for the double slit experiment was expressed as a combination of the single slit data:

$$IG_d = c_1 \cdot IG_s + c_2 \cdot S\{d, IG_s\}$$

Where "d" describes the shift which varies for each baseline as it represents the effective shift introduced in the phase delay to the ZPD which depends on the sine of the angular separation of the two slits times the baseline. The two coefficients contain both aperture relevant effects such as vignetting or differential beam response as well as source unbalance in the case illumination of the mask is non uniform.

But more in general one can adopt (for any 1-D mask) the following:

$$IG_{mask} = \sum_i c_i \cdot S\{d_i, IG_s\}$$

The power of this method is limited to the knowledge of and small modifications of this assumption.

In Grainger et al. we deviated from this assumption by adding a spectral low-pass filter on one of the slits to produce an IG which was the result of the combination of two different spectra sources. In order to retain this method, and test if we could reconstruct what the cut-off frequency of the filter was it was necessary to manipulate the IG in the forward modelling as :

$$IG_{scene} = c_1 \cdot IG_s + c_2 \cdot S\{d, FFT^{-1}[LPF_k(v) \cdot FFT(IG_s)]\}$$

and perform a least-square fit for different values of the frequency cut-off on the above. The result was consistent with the real value of the filter to within the width of the slope of the cut-off.

3.2.2 Monte-Carlo analysis of spatially modulated binned-spectra

By ignoring the prior knowledge of the source and its spectral content we rely on the analysis of the modulation of the spectra (so after the first Fourier transform of the data).

This modulation is calculated by storing in a vector the average value (for each baseline) of the spectra in a given wavenumber (or frequency) bin.

In order to avoid allowing low signal-to-noise portions of the modulated spectrum to have impact on the spatial modulation study, we previously record the areas of the spectra which in the entire set of baselines have high levels of power.

The highest level of power for each bin is then stored in what we refer to as "envelope" spectrum or $S_{max}(v_k) = max(\{FFT(IG_i)\}_i, v_k)$.

These regions of the spectra are then divided in bins with an arbitrary bin size "bsz" which is a trade-off with noise of th spatial modulation (larger bin) and spatial frequency.

A vector we refer to as "spatial" or "G" is then calculated as a function of "cycles" cy

$$G(cy) = \sum_{k \subset bin} \{FFT(IG_i)\}_k / S_{max}(v_k)$$

this will present the spatial modulation present in the data normalized for the maximum value that the spectra assumes at any given spatial modulation.

The latter assumption is of course not ideal, as it assumes that the maximum is recorded (i.e. that we have access in principle to very low baselines – ideally that we have on axis data with no spatial modulation which is what $S_{max}(v_k)$ would record.
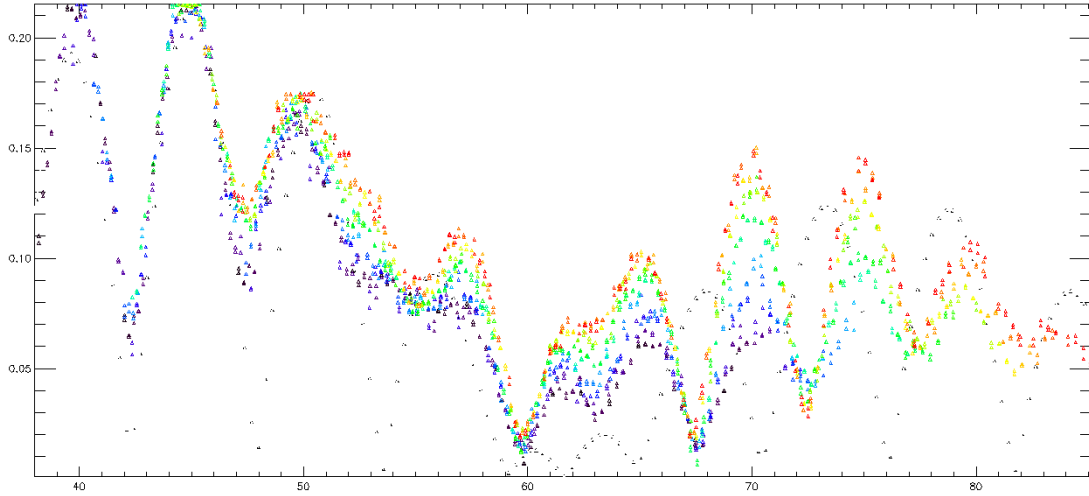
Figure 7. An example of the output of the spatial modulation (each color represents a given spectral bin. The different points for each color is the integral of the spectrum in that bin acquired with a given baseline. Given the definition of the cycles (the x axis) depending on the central frequency of the bin, the x-axis scales for each bin producing the staggered effect of the points in question. (Black is the lowest frequency, thus sensitive to lower spatial scales, varying through blue, green yellow and finally red for the highest number of cycles)

The cycles "cy" in question refer to the fact that each function $G(cy)$ is calculated for a given bin but is plotted against cycles calculated from the vector of baselines and for that specific bin as

$$\{cy_{i,k}\}_{i=1..N} = \{b_i\}_{i=1..N} \cdot v_k \cdot \sin\theta$$

so that each spatially modulated curve can be plotted against a specific set of cycle curves as in Figure 7. v_k is the central frequency of every "k" wavenumber bin. And θ the angle of incidence of the source onto the antennas.

Thus we find ourselves in the position of visualizing Figure 8 a set of clear spatial interference fringes obtained from modulated spectra, but this needs reconducing to an actual spatial structure.

We then proceeded to complete the analysis again with a model fitting which is a step forward from the previous technique but which still depends substantially on prior information about the source adopted.

Specifically we consider a parametric one dimensional model of the aperture mask used. This 1D function is then Fourier Transformed and compared to the normalized spatial modulation.

The Monte-Carlo is then performed allowing the parameters in Table 1 to vary. These have been colour coded to separate those for which we had a safe degree of prior knowledge such that we could fix it and remove the parametric nature of it if needed and those where either no previous knowledge was available or that it was previously

thought unnecessary (but became apparent after noticing that certain spatial modulation features would not be otherwise obtainable).

Table 1. Parameters used in the MC in addition to an arbitrary overall amplitude to account for any residual uncalculated optical efficiencies. The orange parameter is one which is very confident due to the level of precision and stage involved. This is still included as a control tool for the MC. The yellow parameters contain some prior on the actual value while the remaining parameters we have no feel or knowledge for. Bold are the parameters that affect the reconstructed spatial modulated cruves (so these are fit independently as they affect the alignment of the independent spectral bin curves rather than the model fit to them.

Parameter of the MC	Symbol	Initial Value	Estimated Uncertainty	Value Range	Value fit
Initial (min) baseline	b_0	**100 (mm)**	**5 (mm)**	**90 − 110 (mm)**	**103**
Baseline step	db	**3 (mm)**	**0.1 (mm)**	**2.5 − 3.5 (mm)**	**3.0**
Main angle of FoV	θ	0 (rad)	?	0 − 0.02 rad	0.0114
Focal Plane Scale	b_0	1.35 ('/mm)	?	1.0 − 1.5	1.156
Slit separation	d_{sep}	5.5 (mm)	0.3 (mm)	5.0 − 6.0 (mm)	5.95
slit 1 - size	s_1	1.0	0.2	0.5 − 1.5	1.06
Slit 2 - size	s_2	1.0	0.2	0.5 − 1.5	0.90
Slit unbalance	u	0.0	?	0.0-1.0	0.46

The initial baseline is effectively the shortest baseline used (or the offset on the array of baseline values used). The baseline step is set by the scanning step of the linear stage (very difficult for this value to be different from what it was set at). The main angle of the Field of View represents the angle at which the on-axis source is incident on the antennas and is likely to be close to (but strictly greater than) zero. The focal plane scale is imposed by the telescope design and any variation is likely to be due to de-focusing introduced by incorrect positioning or deviations of the mirro from its nominal shape. The slit separation is well measured, but it is allowed to vary due to the potential difference in value arising from different illumination distribution behind the slits. The relative size of the slits is partially degenerate with the slit unbalance, but has spatial implications due to the actual sizes involved (the f.p.s.). Finally the slit unbalance or the overall strength of the source behind the each of the slits.
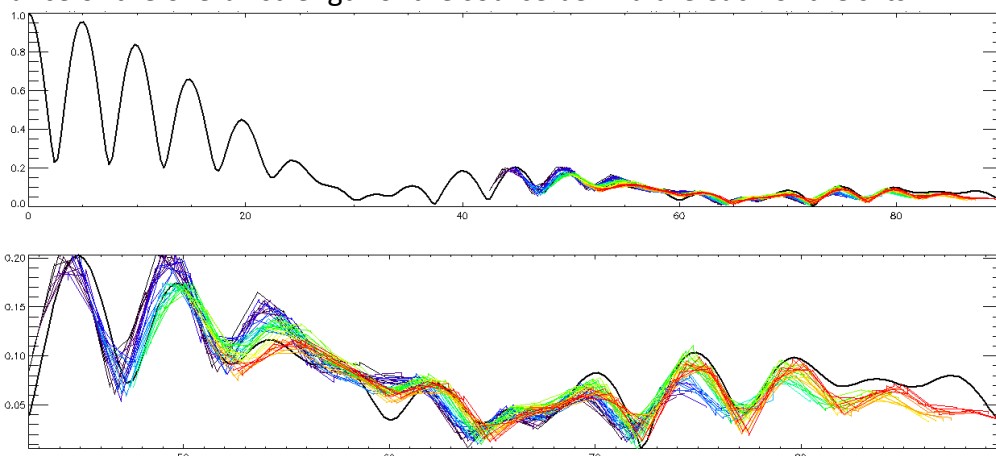
Figure 8. Model fit to spatial modulation curves. Above the spatial FT of the scene which best fits the combined spatial modulation of the data is shown from the zero point (on-axis). The correspondence to relatively high cycles interval is due to the off-axis set-up of the source with respect to the telescope focus. The combination of this position and the focal plane scale (f.p.s) is degenerate with

**the theta angle fit. Below, the region where the spatial modulation of the spectra occurs. The curves
are consistent with the combined modulations.**

The resulting fit can be seen in Figure 8 and is far from perfect. It is possible that a few
additional factors require taking into account (see Section 5).

However the step forward from the previous analysis is inherent to the number of
additional parameters required (not superfluous) to improve the overall fit of the
curves. Some effects observed (such as the non-zero reaching destructive interference
fringes caused by the two independent slits (while the slower modulation does)
suggested we include the slit illumination non-uniformity (unbalance) rather than the
antenna or beam-splitter unbalance.

3.2.3   Cosine transform of the interpolated modulated spectra

Here we briefly point out our next efforts in performing the analysis will consist of a set of
direct Cosine transforms of the curves plotted in Figure 8. These would then require phasing
of some kind in order to properly position within the Filed-of-view.

For this reason either reference known sources could be used (i.e. a small portion of the mask
used as a reference or spatially separated bias) or an equivalent of the CLEAN algorithm could
be investigated to combine in first instance the combined spectral content to guide the
phasing of the spatial information contained in the different spectral bins.

The generic formula applied in this case to the "dirty" spectra (which we have referred to as
spatially modulated spectra) is the 1D form of Eq. 5.6 of [2] which we reproduce modified for
clarity

$$Scene(\theta; v_k) = \sum_{j=1}^{N_b} \left| \Re\{S_p(v_k; b_j)\} \cos[2\pi(u_{j,k}\theta)] - \Im\{S_p(v_k; b_j)\} \sin[2\pi(u_{j,k}\theta)] \right|$$

where $u_{j,k} = b_j v_k$ are the spatial frequencies.

4 Detailed optical model of the testbed and implications for spectral-spatial interferometry

4.1 The testbed optical model

Optical modelling of the testbed was carried out using one of three propagation techniques. For detailed analyses at these operating frequencies (150 GHz - 3.3 THz), where component sizes are not very large compared with the wavelength of radiation, techniques that consider the vector nature of electromagnetic field are used. We use vector physical optics implemented in either the commercially available GRASP[1] software or the in-house modelling software MODAL [3]. At the highest frequencies, where components are electrically large, this technique becomes impractical (and unnecessary) to carry out and we can take advantage of the speed of geometrical optics (ray-tracing) as implemented in the Zemax[2] optical modelling package. At intermediate frequencies we often make use of Gaussian beam mode modelling [4]. This paraxial technique treats the electromagnetic field as scalar (so each polarisation must be modelled separately) but does take diffraction into account.

---

[1] TICRA Engineering Consultants, http://www.ticra.dk/ (as of August 2015).

[2] Zemax-EE, ZEMAX Development Corporation, http://www.zemax.com/ (as of August 2015).
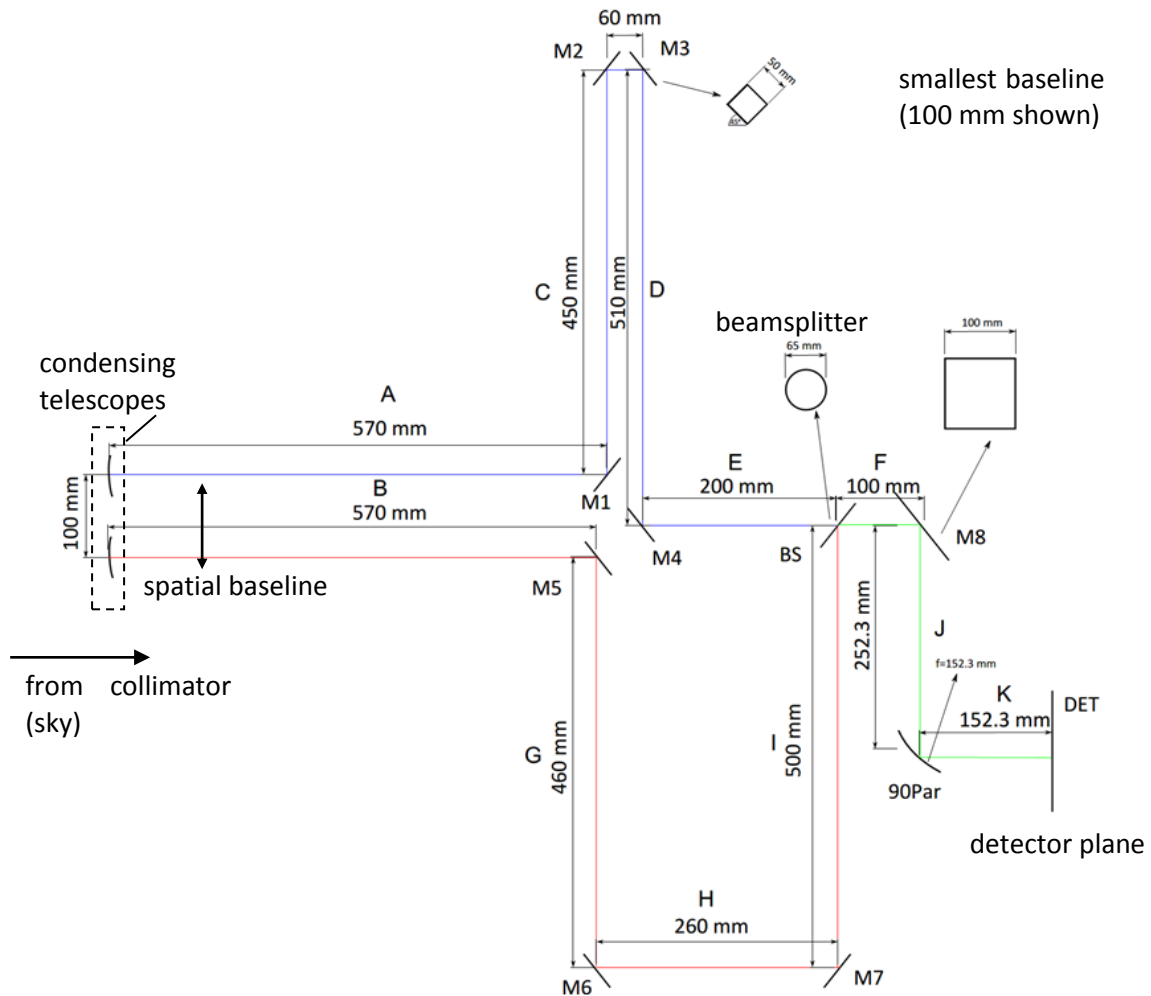
Figure 9. Layout of the interferometer optical model. With the exception of the off-axis parabolic mirror in front of the detector, all mirrors are flat. In an early version the flat mirrors had a square aperture, in the current version they have a circular aperture.

We use each of these techniques to propagate an optical beam through our model of the Cardiff test bed. The layout of the optical model of the interferometer arms, and our component naming convention, is shown in Figure 9.

A source scene is observed by the interferometer via two condensing telescopes (Figure 10). One beam is sent to the spectral arm labeled A. The length of path C and D can be increased or decreased to produce a time delay in one optical path by adjusting the position of elements M2 and M3. The other beam is sent to the spatial arm labeled B. The separation between the condensing telescopes can be adjusted by changing the position of element M5 thereby reducing the length of path G. Both beams are combined at the beamsplitter (BS) and sent to a detector at DET.

Depending on the particular aspect being studied, our model source beam could be either the beam of the detector coupling horn (Winston cone, or a Gaussian approximation) which is propagated through each arm of the interferometer (independently), through the condensing telescope and on to the sky (i.e. the far-field) or it could be the beam produced by the test-bed source which is propagated to the collimator and then through the telescopes and interferometer and then on to the detector plane.
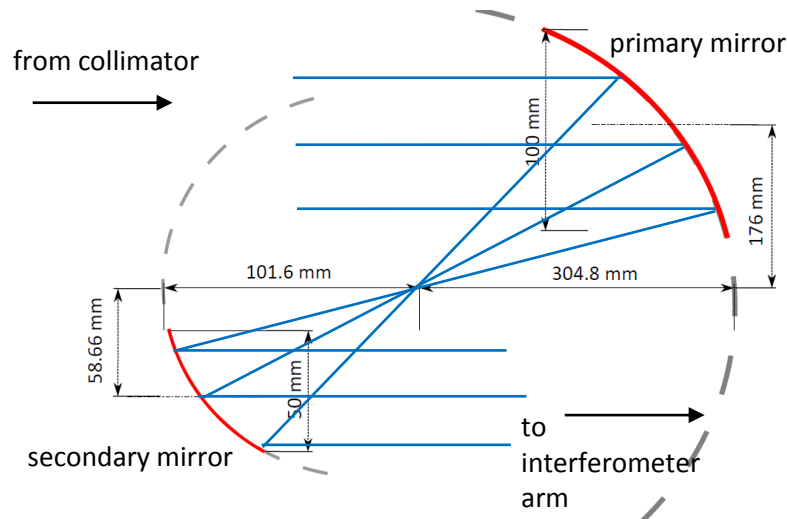
Figure 10 Model of the 3:1 condensing telescope (out of the plane of the diagram in Figure 9). Each mirror is an off-axis section of a parent parabola.

4.2 The effect of diffraction

4.2.1 Diffraction and truncation in the laboratory testbed

A Gaussian beam mode analysis was carried out in order to assess the effects of beam diffraction and truncation across the band of interest (90 - 2000 μm, 0.15 - 3.3 THz). Figure 11 shows the change in beam radius of a Gaussian beam propagating through an on-axis approximation of a testbed arm. It is clear from this analysis that, at the long-wavelength end of the band, diffraction is significant and the resulting increase in beam radius as a function of propagation distance leads to the beam being truncated at optical elements in its path. At the high-frequency end of the band there is little truncation and the beam size could have been predicted using geometrical optics.

Physical optics was used to determine the beam amplitude and phase at each optical component and at several wavelengths across the band. Amplitude results for the smallest spatial baseline are shown in Figure 12. Diffraction and truncation can be seen to affect the amplitude distribution across each beam and so their effect on recovered spectra should be assessed (section 4.2.2).
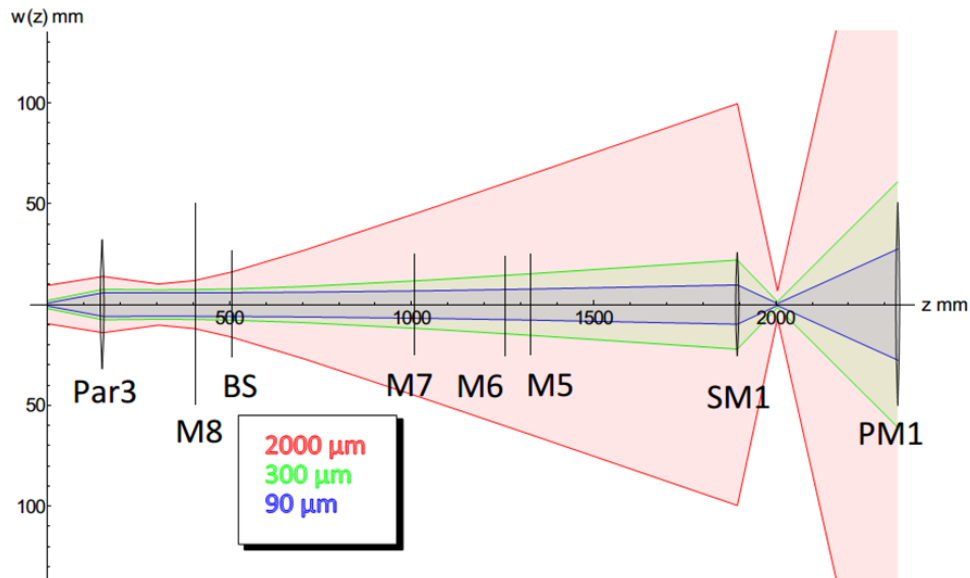
Figure 11. Beam radius as a function of propagation distance in an interferometer arm (arm B in Figure 9). An on-axis approximation of the system is used.
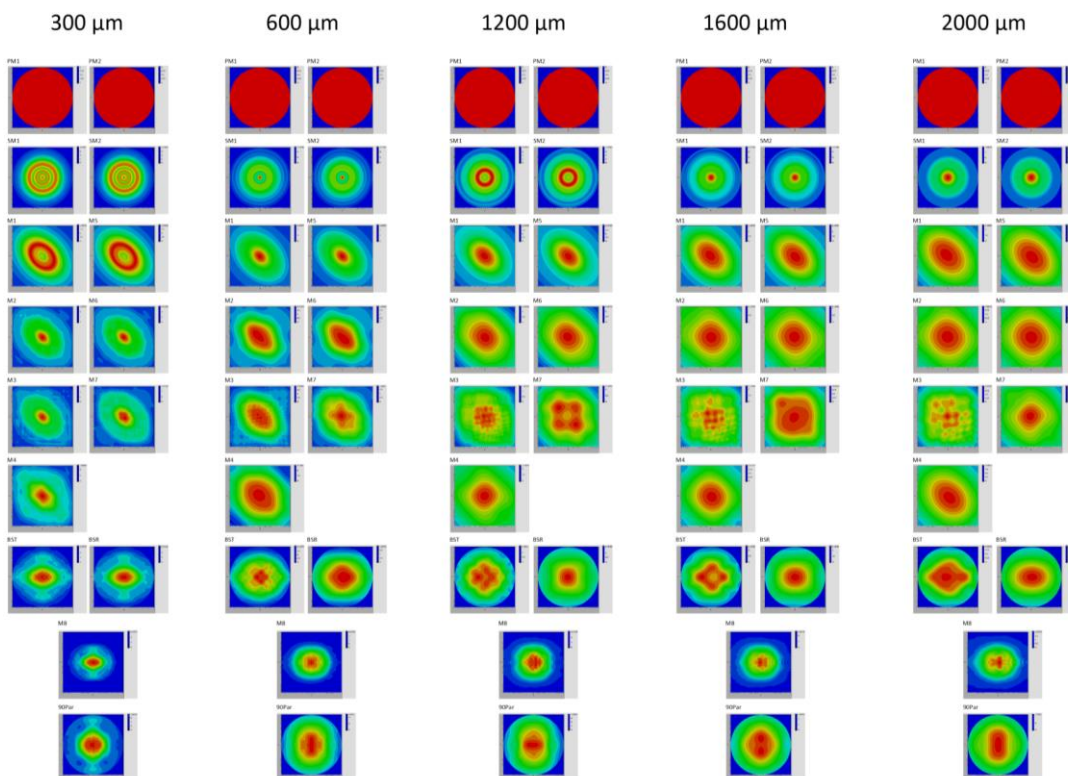
Figure 12. Physical optics simulation of beam amplitude at optical components in the testbed (both arms are shown, the top line is at the primary mirror, the next at the secondary etc.). In this case the source was taken as a plane wave at the condensing telescopes and this was propagated through the interferometer and on to the detector plane. The two beams were added at the beamsplitter to give the combined beam at the final two surfaces.

4.2.2 Simulation of fringes

A model of the testbed was constructed in MODAL with a plane wave incident at the primary mirror of each condensing telescope. Five wavelengths were selected for the simulation: 300, 325, 350, 375 and 400 μm. The shortest baseline (100 mm) was used as this corresponds to the longest propagation distance in the interferometer arms. A beam was propagated through each arm of the test bed using physical optics and the total power at the detector plane was calculated. This process was repeated with varying lengths of the spectral arm as follows. Beginning at 0 path length difference and increasing the length of the spectral arm in steps of 12.5 μm, 101 samples were taken. Then beginning at -12.5 μm and decreasing the length of the spectral arm in steps of 12.5 μm m, a further 100 samples were taken. The entire process was repeated for all five wavelengths. and the resulting fringe patterns are shown in Figure 13.
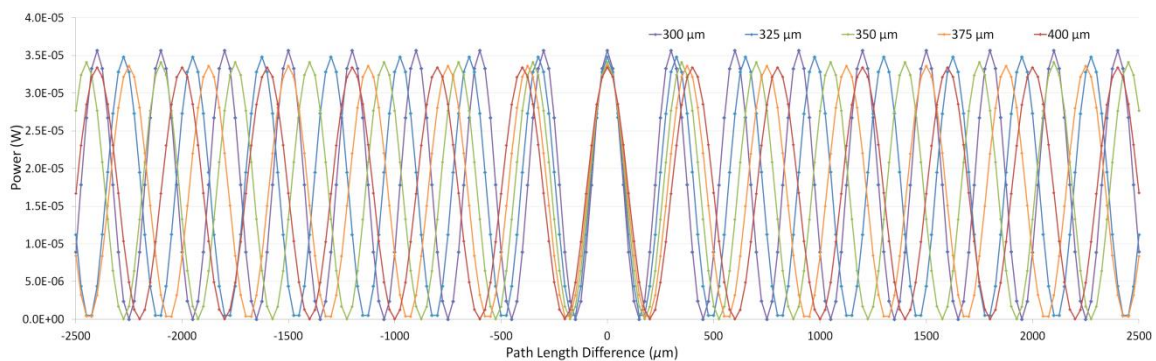
Figure 13. Total power on the detector plane as a function of path length difference for five wavelengths. A plane wave (point source on the sky) was used as input at the condensing telescopes. 201 simulations were carried out at each wavelength for path length differences ranging from -2500 μm to +2500 μm.

The fringe patterns were weighted to simulate a Gaussian input spectrum and then summed to give the interferogram in Figure 14. In the absence of diffraction and truncation, an intensity pattern of the form

$$I(\delta) = I_0 \left(1 + \cos \frac{2\pi}{\lambda} \delta \right), \tag{1}$$

where δ is the path length difference, should result at each wavelength giving an ideal interferogram also shown in Figure 14. The patterns are very similar although the diffraction, off-axis aberrations, truncation etc. accounted for in the physical optics model do reduce the fringe visibility slightly.

A discrete Fourier transform of the data was carried out to recover the spectra in Figure 15. The Gaussian spectral shape was recovered in both cases. While the effects modelled here might not be the most significant source of error in the laboratory testbed, they are at a level that should be considered in the overall error budget of a space mission.
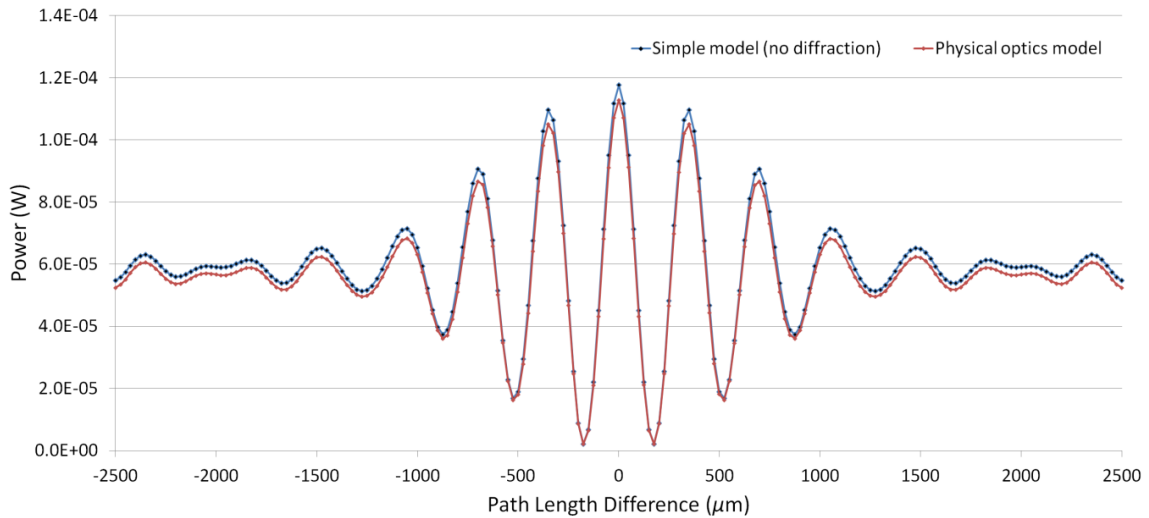
Figure 14. (red) The interferogram resulting from the summation of the five fringe patterns shown in Figure NUIM5. (blue) The ideal interferogram at the same five frequencies if optical effects (diffraction, truncation, aberration) are ignored.
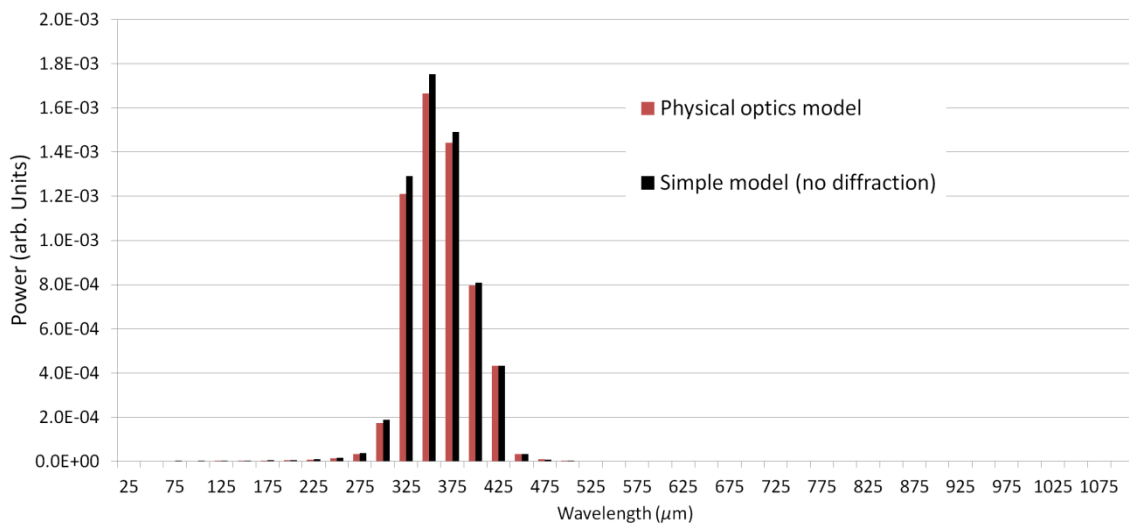
Figure 15. Spectrogram obtained by a discrete Fourier transform of the interferograms of Figure 14 (intensity in arbitrary units). Both the physical optics model and the ideal model (no diffraction, truncation, aberration) are shown.

4.3   The effect of aberrations

Next we investigated the effect that aberrations introduced into the beam could have on the fringe visibility. The beam splitter was considered to be the most likely element to contribute significant aberration and so we decided to artificially introduce aberrations at this point (we had no measurements to indicate that the beam splitter did distort the beam in this testbed). Fringe patterns "on the sky" were calculated by propagating a source beam from the detector plane, through the interferometer and condensing telescopes and then through a collimating mirror to a test plane at its focus in order to simulate propagation to the far-field (as is the case in the laboratory testbed).

The source beam to use was first found by propagating a plane wave incident on the collecting telescopes through the interferometer and on to the detector plane. The best-fit Gaussian beam to this detector field was then taken as the source beam. This new source was propagated from the detector plane back through both arms of the interferometer and the collimating mirror onto a test surface. At the location of the beamsplitter an astigmatic aberration of the form

$$z = a(1 \times 10^{-4} \text{ mm}^{-2})(x^2 - y^2) \tag{2}$$

was added to the beam amplitude in one arm (B), where x and y are coordinates in the plane perpendicular to the direction of beam propagation (Figure 16). This particular shape of distortion was taken as an example simply to assess levels of visibility loss that could be result in typical systems.
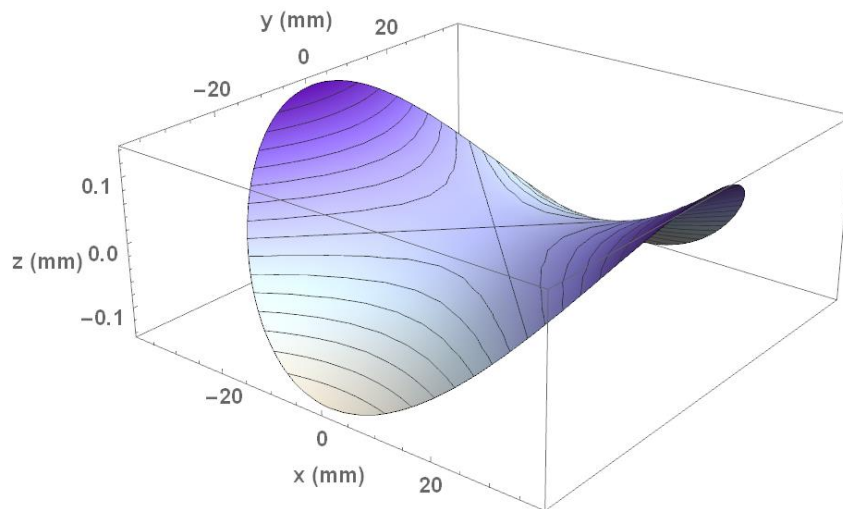
Figure 16. The astigmatic distortion added to the beam in one interferometer arm.
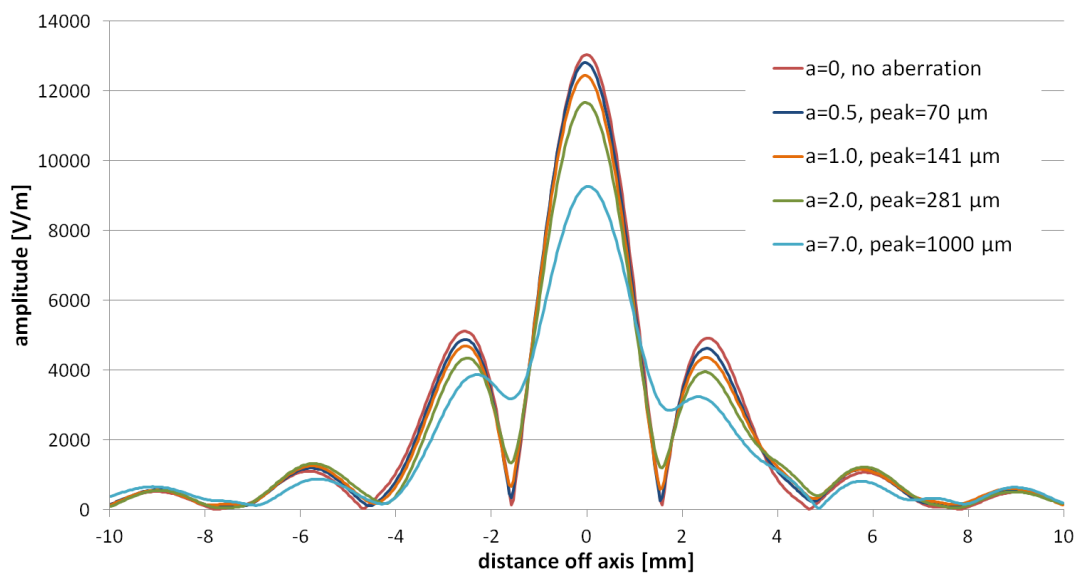
Figure 17. The fringe patterns produced when an astigmatic amplitude aberration is introduced into one arm of the interferometer, operating at $\lambda = 300 \ \mu m$. The aberration was of the form given in Equation (1) with $a = 0, 0.5, 1.0, 2.0, 7.0$.

Figure 17 shows an example of the fringe pattern results in the case of $\lambda = 300 \mu$m. We can estimate the visibility from the maximum and first minimum values of this pattern $((I_{max} - I_{min})/(I_{max} + I_{min}))$. The results show that amplitude aberrations should be significantly smaller than a wavelength in order to avoid visibility losses of a few percent. We would expect that a fixed amplitude distortion would have a decreasing effect as the operating wavelength is increased. However this was not the case for the shortest wavelengths and smallest distortions investigated (Figure 18). The propagation distances in the interferometer are such that depending on the wavelength (the confocal distance $z_c = \pi w_0^2 / \lambda$), optical components may be in the near- or far-field and this must be taken into consideration when extrapolating trends. In the case of small distortions it is difficult to measure small visibilities accurately from plots such as those in Figure 18 without very fine sampling near maxima and minima. We did notice that even with no aberrations added we did not recover a visibility of close to 1, despite the beam patterns at the two condensing telescopes being very similar (coupling >0.999). This led us to investigate the role of the collimating mirror, discussed next.
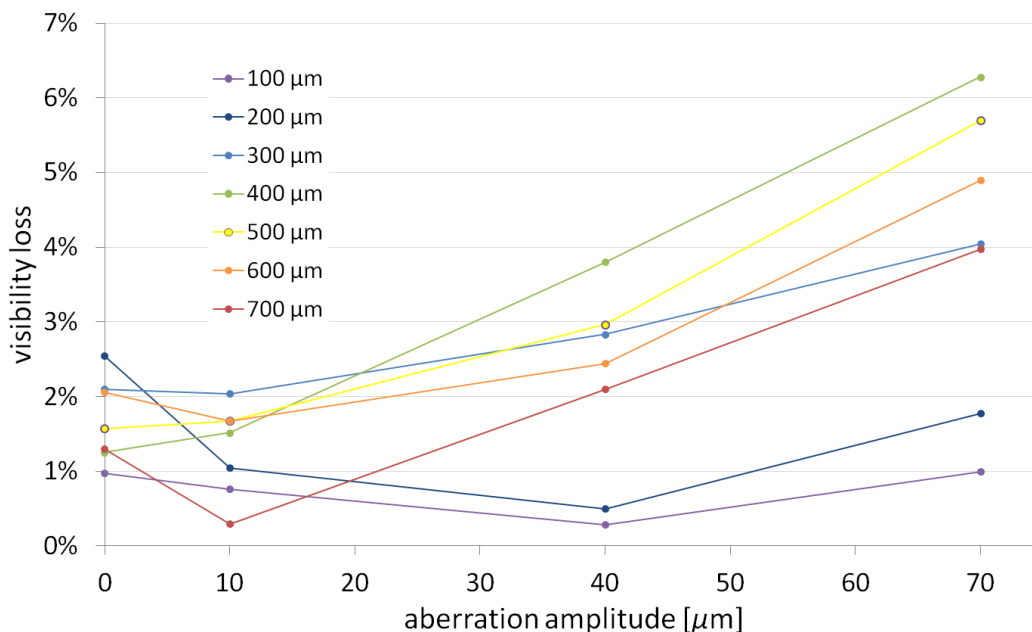
Figure 18. Percentage visibility loss as a function of aberration amplitude (141a μm) at different operating wavelengths.

4.4   Sky-Simulator Collimator

The testbed built at Cardiff University consists of two main parts: a source simulator and the spectral spatial interferometer (Figure 19). The source simulator uses a large collimating mirror, which (for a point source) produces a flat wavefront at the two collecting telescopes of the interferometer, simulating what would be received from a real astronomical source at infinity. From the results in Section 4.3 we can see that the source simulator (not present in an astronomical mission) does have an effect on the modelling results. We investigated the possibility of improving the testbed by replacing the spherical collimating mirror with a parabolic mirror, which would be better able to produce plane waves to represent a point source on the sky.
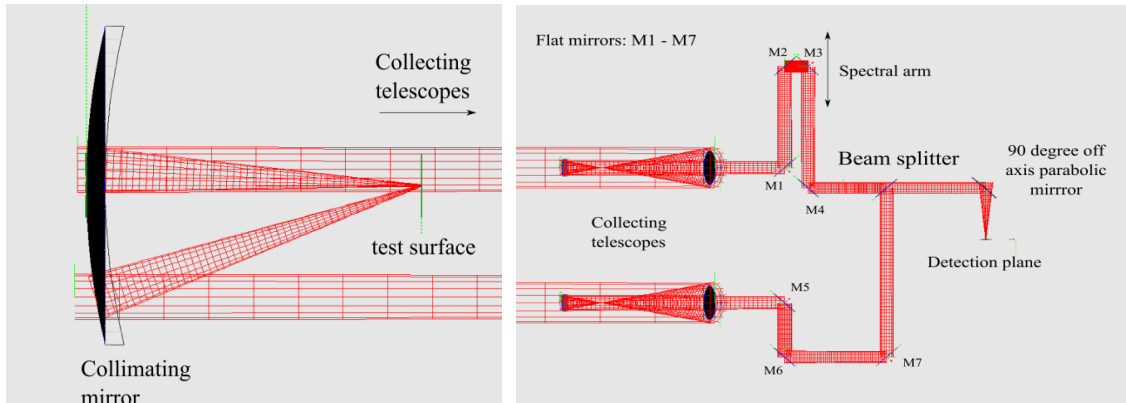
Figure 19. (left) The source simulator and (right) interferometer arms of the Cardiff University spectro-spatial testbed as set up in the MODAL modelling package.

A model of a Gaussian source was created at the focus of the collimating mirror. Its waist of 0.27 mm yielded a beam radius of 0.5 m at $\lambda = 400\ \mu$m by the time it reached the collimator. The electric field structure of the beam was analysed at the plane where the collecting telescopes are located. In order to vary the interferometer baseline, the position of one of the collecting telescopes was moved while the other was kept constant (as is the case with the real Cardiff University system). This analysis was carried out for the existing spherical collimator and also for a re-designed parabolic mirror.

Figure 20 shows the phase of the electric field across the on-axis and a 400-mm off-axis collecting telescope for a beam propagated from a spherical and a parabolic collimating mirror. At short baselines there is very little difference between the spherical and parabolic collimators. However, Figure 20 clearly shows that at the longer testbed baselines the spherical collimator does indeed give rise to a significant slope in phase across the off-axis collecting telescope. The parabolic collimator also exhibits some level of slope in phase, but it is significantly lower than for the spherical mirror.
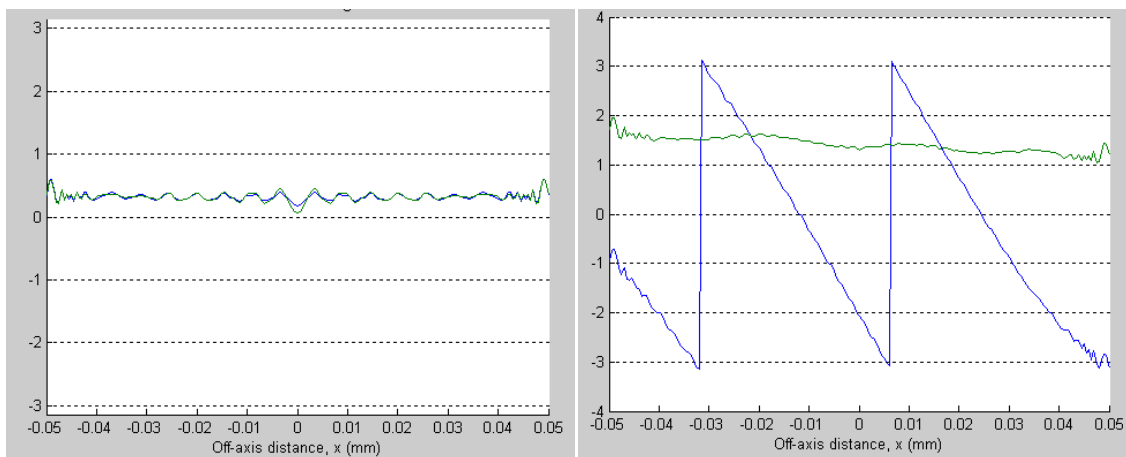
Figure 20: Phase (rads) of the electric field across an on-axis (left) and 400 mm off-axis (right) collecting telescope, for a beam propagated from a spherical (blue) and a parabolic (green) collimating mirror.

We continued the investigation by modelling the fringes that would be produced from the testbed using these collimating mirrors. A Gaussian beam was propagated from the detector plane through the entire system and focused by the collimating mirror onto a test surface. Both mirrors produced a similar fringe pattern with good visibility when the baseline was 100 mm, however, when the baseline was set to 400 mm the fringe pattern produced by the spherical mirror was much less well defined compared to that produced by the parabolic mirror (Figure 21). It can therefore be concluded that replacing the spherical with a parabolic one would likely yield a significant improvement in fringe recovery results.
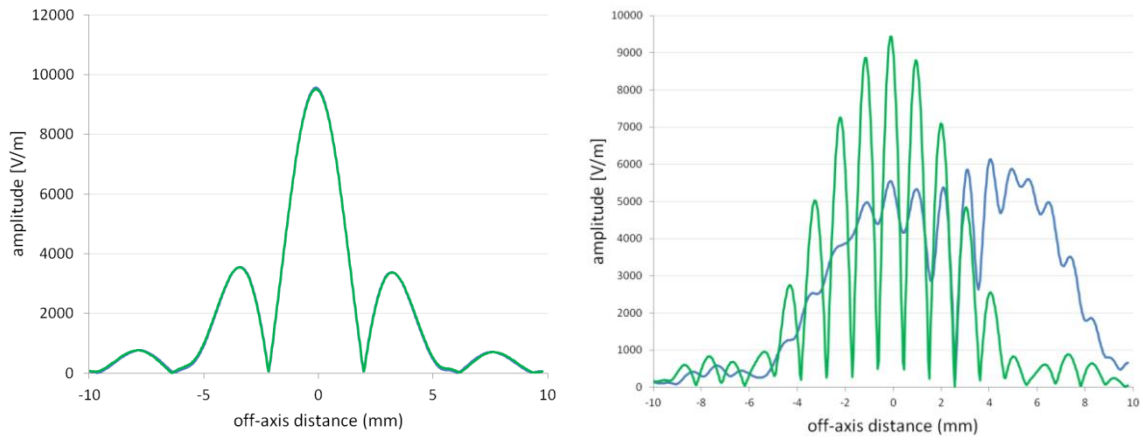
Figure 21: Fringes produced at the focus of the collimating mirror for a (left) 100-mm and a (right) 400-mm baseline when a spherical (blue) and a parabolic (green) mirror is used as the collimator.

4.5   Tolerance Analysis

We analysed the tolerance of the testbed system to misalignments in the system, in particular to see if the loss of power with increasing baseline length reported by Grainger et al. [5] could be explained. Figure 22 shows that misalignments in the roof mirror on the order of a degree could cause a large loss in the power measured at the detector plane and that this loss increases with increasing baseline length.
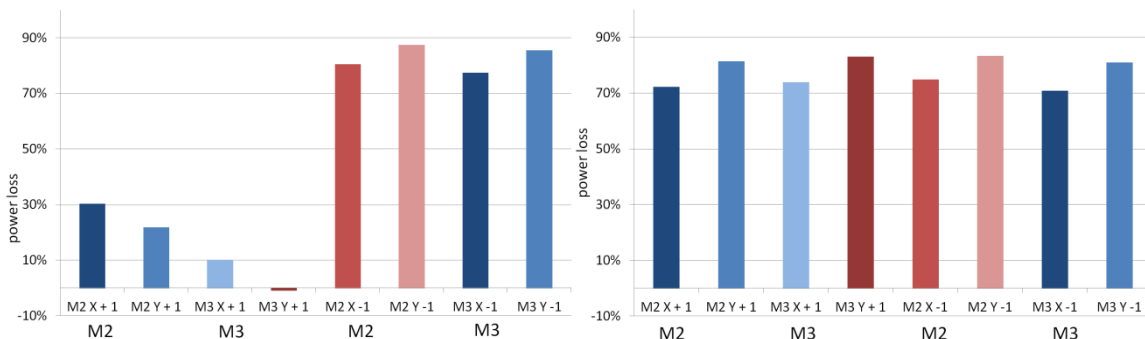
Figure 22 The percentage of power lost when the roof mirrors in the spectral arms are mis-aligned by 1 degree for the (left) shortest100-mm and (right) longest 50-mm testbed baseline.

We also investigated the alignment requirement for the collecting telescopes if no more than 5% of the power is to be lost. We used MODAL to predict the power loss for a discrete set of misalignments about 3 axes. Our results show that the required pointing accuracy of the condensing optics is ± 0.025° to avoid a power loss of more than 5% (Figure 23).
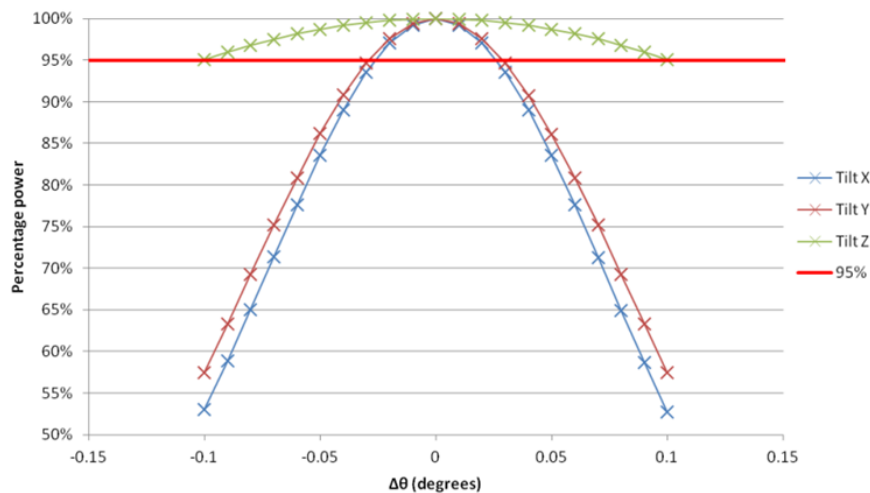
Figure 23. Power at the detector plane as a function of primary mirror misalignment (about each of three axes) in the collecting telescopes

4.6 Future Upgrades and Conclusions

In this section we have used optical models of the Cardiff University testbed to analyse the effects of long-wavelength operation, non-idealities such as mis-alignments aberrations and truncations and the use of a spherical collimating mirror to simulate astronomical sources. The collimating mirror is specific to laboratory testbeds but the other analyses should be useful when considering the design of long-wavelength interferometers for space in general.

The spreading of beams at the longest of the testbed wavelengths gives rise to significant truncation and loss in power. When the full band is considered the effect on the recovered spectra is small, though wavelength-dependent. It should be considered in a real instrument when a detailed spectral analysis of sources in required. Aberrations, unless they are of an amplitude of about an order of magnitude smaller than the wavelength could on the other hand cause a significant reduction in fringe visibility of the testbed. Since the distances between optical components in the testbed can be either in the near- of far-field of beams, depending on which end of the band is being considered, it can be difficult to predict trends with wavelength without doing a proper analysis.

The optical modelling has shown that accurate alignment of the components, in particular the roof-mirrors, is very important at the long baselines. Replacing the spherical mirror in the collimator with a parabolic on would also make it easier to recover fringes at long baselines.

5 Spectral-spatial information recovery and non-ideal system effects

Witnessing the double fringe modulation on the recovered and analysed data from the spectral-spatial interferometric testbed yields an immediate (almost satisfactory) recognition of the process which is taking place. The clarity of this double modulation though is subsequently replaced with the frustration (common of many other physical processes) of finding a close enough model to explain and describe this behavior in detail.

What follows is a qualitative attempt to associate a number of specific effects which can be present in the testbed and thus affect the data acquired. We describe in detail why such effects were considered to be most likely to impact the data and at what level. In each case we address if these present an issue for future testbeds or instruments or if they can be overcome.

The following subsections, follow the same order of section 2 to look in how these can affect the data in question.

5.1 The source

We have observed how the positioning of a mask does not have the final word in defining the source given the actual location in space of the focus of the mirror.

Any source adopting a mask for spatial definition should be positioned very close to it. An alternative for high levels of signal which can afford to reduce the input power is to include diffusing substrates in the open parts of the mask.

Emitting sources directly spatially defined have less issues of this kind (albeit usually much less emitted power).

A comprehensive review of sources and their nature is contained in D.3.5 from this same project.

Another point to be kept in consideration is the wide-angle beam nature of a small antenna that can be employed for a testbed. As such, case should be taken in limiting input angles at any image plan through the system to avoid contamination from other bright sources in the beam side-lobes.

5.2 The collimator

Much has been said of the collimator in Section 4, to which we refer here. Most phase issues are controlled in the design of the optical system.

One particular temptation which must be avoided is the deformation or optimization of the mirror alignment in terms of its mount or actuators to maximize the signal received, when this is a combined alignment issue of the positioning of the source in the collimator focus and the overall alignment of the testbed antennas. Deformations of the primary can be difficult to correct in post-processing and should be avoided.

5.3   The telescopes (antennas)

The antennas offer a few possible effects as impact to the testbed data.

Differential beam-shape or size caused by non-identical mirrors or positioning of such mirrors, can produce a small unbalance of the power in the two antennas, this is a marginal error. A difference in pointing between the two antennas can, in a similar way, imply a different weight being assigned to the incoming source even in the case of identical beams.

Beam condensation should also usually be adopted with caution given that there is a trade-off in attempting to increase the size of the antennas to increase the receiving power and avoiding excessively large angles resulting from a high ratio of collimated beam condensation resulting in subsequent loss during the collimated beam propagation.

5.4   The delay stage

The delay stage is often considered as the main culprit of many phase errors and other artefacts. The specific case of high-sensitivity instruments such as the Herschel SPIRE-FTS where many small effects were observed and the nuances of a non-ideal delay stage are discussed in another deliverable (D.3.6). In our case, the upgrade to the new stage resolved most issues with tolerances way above the level necessary to impact observations at these wavelengths.

We refer to the other documentation for a detailed discussion of such effects, but here we can mention that non-uniform scanning speed or other errors which can originate from errors in the closed-loop control which depends on a gauge and its sensitivity to temperature are all effects which can have impact on the data. This testbed in particular has not yet reached this level.

5.5   The beam combiner

The beam combiner details (discussed in D3.2) possess the capability of not only unbalancing the beam (given the R/T properties) but also that of introducing a phase delay inherent to the reflection and transmission of the two sides of the device.

Fortunately though this effect (which has an impact when trying to retrieve the exact ZPD of a system given that this phase delay can and most likely depends on frequency) is at least constant.

A study to detail the impact of these effects would not be excessively complex and would require assembling the detector on the other output port of the combiner and observe the differences in phase with respect to the original configuration when presented with data taken in the exact same manner.

5.6   The detector

Detectors come in different forms and it is not the scope of this document to delve in the different issues that different technologies have in their implementation for a testbed such as this one. It is however implicit that one of the biggest issues with general photometry is that of non-linear behaviour.

In Fourier transform spectroscopy, non-linear behaviour has one advantage of being relatively "easy" to identify given that it manifests itself in replications at higher frequencies of the original spectra features. Of course this has the potential of confusing the observer in the spectral retrieval, but changing the Nyquist frequency for similar experiments usually suffices to identify them (while removing the effects is altogether a different matter).

Combining this effect with spatial modulation is however a test we have not yet been faced with given the linearity of the detectors used. The very planning of this deliverable was initially due to the expectation of observing such features. Future experiments could attempt to increase power levels substantially to generate non-linearities.

6 Future suggestions and planned work in the post-FISICA era.

In this document we have briefly outlined a number of effects which illustrate how the spectral-spatial interferometry testbed deviates from an ideal performance. At the same time, the results obtained and the elements which can be inferred by some of these results allow us to contemplate how the system is working and can be improved. A number of these improvements have been outlined in the previous chapter, with the upgrade of the collimator and added metrology to the testbed.

Complex sources and a rotating mask will allow extension of these considerations as well as data analysis algorithms to the 2D case.

In addition the forthcoming campaign of the BETTII Experiment due to launch in 2016 will provide opportunity to compare some of the analysis performed and issues observed to real data and support in its analysis.

7 Bibliography

[1] P. A. R. Ade, "Progress in Spectral-Spatial interferometry at multi-THz frequencies - Potential applications," Cardiff, 2015.

[2] R. Juanola-Parramon, PhD-Thesis "A Far-Infrared Spectro-Spatial Space Interferometer: Instrument Simulator and Testbed implementation", London: Springer, 2014.

[3] M. Ł. Gradziel, "Modelling of the optical performance of millimeter-wave instruments in MODAL," in *SPIE*, 2007.

[4] P. Goldsmith, Quasioptical Systems: Gaussian Beam Quasioptical Propagation and Applications., IEEE Press series on microwave technology and techniques., 1998.

[5] W. F. Gringer, "Demonstration of spectral and spatial interferometry at Thz frequencies.," *Appl. Opt.,* p. 51, 2012.